Generation of quantum phases of matter and finding a maximum-weight independent set of unit-disk graphs using Rydberg atoms

Ahmed M. Farouk [1,2,3,*] I. I. Beterov [2,4,5,6,†] Peng Xu [7,8] and I. I. Ryabtsev [2,4]

[1]*Faculty of Mathematics and Mechanics, Novosibirsk State University, 630090 Novosibirsk, Russia*
[2]*Laboratory of Nonlinear Resonant Processes and Laser Diagnostics, Rzhanov Institute of Semiconductor Physics SB RAS, 630090 Novosibirsk, Russia*
[3]*Department of Mathematics, Faculty of Science, Al-Azhar University, 11884 Cairo, Egypt*
[4]*Faculty of Physics, Novosibirsk State University, 630090 Novosibirsk, Russia*
[5]*Department of Laser Physics, Institute of Laser Physics SB RAS, 630090 Novosibirsk, Russia*
[6]*Faculty of Physical Engineering, Novosibirsk State Technical University, 630073 Novosibirsk, Russia*
[7]*State Key Laboratory of Magnetic Resonance and Atomic and Molecular Physics, Innovation Academy for Precision Measurement Science and Technology, Chinese Academy of Sciences, Wuhan 430071, China*
[8]*Department of Quantum Computing, Wuhan Institute of Quantum Technology, Wuhan 430206, China*

(Received 16 May 2024; revised 5 July 2024; accepted 9 August 2024; published 27 August 2024)

Recent progress in quantum computing and quantum simulation of many-body systems with arrays of neutral atoms using Rydberg excitation has provided unforeseen opportunities towards computational advantage in solving various optimization problems. The problem of a maximum-weight independent set of unit-disk graphs is an example of an NP-hard optimization problem. It involves finding the largest set of vertices with the maximum sum of their weights for a graph which has edges connecting all pairs of vertices within a unit distance. This problem can be solved using quantum annealing with an array of interacting Rydberg atoms. For a particular graph, a spatial arrangement of atoms represents vertices of the graph, while the detuning from resonance at Rydberg excitation defines the weights of these vertices. The edges of the graph can be drawn according to the unit-disk criterion. Maximum-weight independent sets can be obtained by applying a variational quantum adiabatic algorithm. We consider driving the quantum system of interacting atoms to the many-body ground state using a nonlinear quasiadiabatic profile for sweeping the Rydberg detuning. We also propose using a quantum wire, which is a set of auxiliary atoms of a different chemical element, to mediate strong coupling between the remote vertices of the graph. We investigate this effect for different lengths of the quantum wire. We also investigate the quantum phases of matter realizing commensurate and incommensurate phases in one- and two-dimensional spatial arrangements of the atomic array.

DOI: 10.1103/PhysRevA.110.022442

I. INTRODUCTION

In the realm of computer science [1] there is a class of nondeterministic polynomial-time NP-hard problems that are notoriously challenging to solve efficiently. The algorithms designed for classical computers struggle to find solutions of such problems within a reasonable time frame or cost. With the development of the capabilities of quantum computing technologies there is a growing interest in finding useful applications of near-term quantum machines [2]. Recent achievements in this field have allowed further exploration of the possibility of finding solutions of a number of NP-hard problems [3]. In particular, recently it has been proposed to implement a quantum annealer with heteronuclear ultracold Rydberg atoms in optical lattices, featuring a highly controllable environment to explore the many-body adiabatic passage [4].

In graph theory [5] we define a graph $G(V, E)$ with V the set and E the edges. A graph is called planar if its vertices are embedded in the plane and its edges are not intersecting. Nonplanar graphs represent a class of graphs where the edges between some of the vertices are intersecting and the vertices can be represented in three-dimensional space. A subset S of a set V is called an independent set if there are no couples of vertices of S which are connected by the edge E. If there is no larger independent set S' with $|S'| > |S|$, then S is a maximum independent set (MIS). In other words, the size of the maximum independent set is the cardinality (number of vertices) of the largest independent set of the graph. Assigning a weight $w_v > 0$ to each vertex $v \in V$ generalizes the MIS problem to a maximum-weight independent set (MWIS) problem, which can be solved by finding the independent set with the total weight $W = \sum_{v \in V} w_v$. Finding the solution for the MIS or MWIS is an NP-hard problem [1], meaning there is no known efficient algorithm to solve it for all possible graphs. However, there are approximate classical algorithms and heuristics that can provide good solutions in practice. Examples of weighted graphs considered in our work are presented in Fig. 1(a).

Different approaches related to quantum computing can be used to solve both MIS and MWIS problems. Basically, there are two main approaches to driving the quantum system to the many-body ground state, which reveals a solution for MIS,

*Contact author: ahmed.farouk@azhar.edu.eg
†Contact author: beterov@isp.nsc.ru

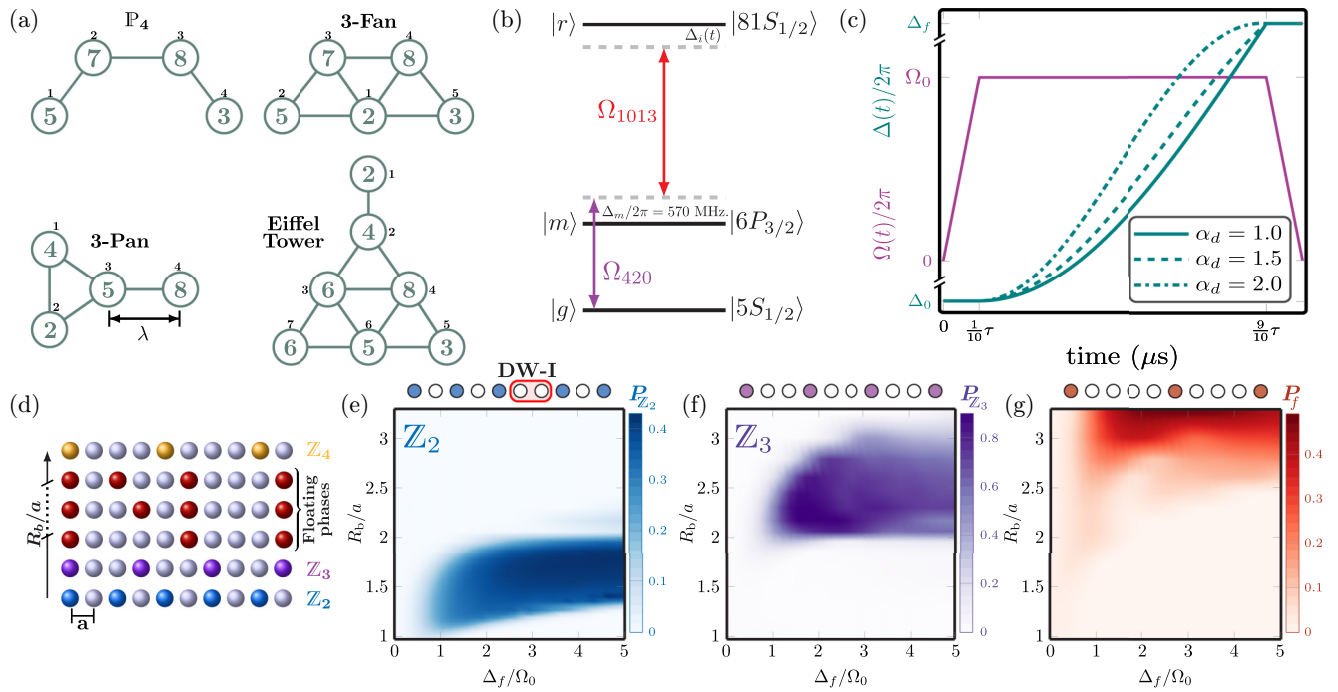

FIG. 1. (a) Arbitrary undirected planar graphs being represented by Rydberg atoms. The positions of the vertices are defined as a function of graph spacing constant λ in Table I. The labels inside the circles represent weights of the corresponding vertices. The numbers outside the circles mark the position of each vertices. (b) Scheme of the atomic energy levels and laser excitation scheme for ^{87}Rb atoms. (c) Time profiles of two-photon Rabi frequency $\Omega(t)$ and detuning from the Rydberg state $\Delta(t)$ for three different laser excitation courses with parameters α in Eq. (5): $\alpha_d = 1.0$ (teal solid curve), $\alpha_d = 1.7$ (teal dashed curve), and $\alpha_d = 2.0$ (teal dash-dotted curve). Here $\Omega_0/2\pi = 1.75$ MHz, $\Delta_0/2\pi = -6.0$ MHz, $\Delta_f/2\pi = +6.0$ MHz, and $\tau = 5.0$ µs. (d) Scheme of quantum phases of matter represented by Rydberg excitations in the atomic array (shown as colored circles) with commensurate orders $\mathbb{Z}_2$, $\mathbb{Z}_3$, and $\mathbb{Z}_4$ and possible incommensurate floating phases between $\mathbb{Z}_3$ and $\mathbb{Z}_4$. Numerically calculated probability distributions (e) $\mathbf{P}_{\mathbb{Z}_2}$, (f) $\mathbf{P}_{\mathbb{Z}_3}$, and (g) $\mathbf{P}_f$ are plotted for ordered states $\mathbb{Z}_2$ and $\mathbb{Z}_3$ and an incommensurate floating phase, respectively, for an array of ten atoms arranged in one dimension with lattice spacing constant a (µm). The red rectangle on top of graph (e) marks the position of a domain wall.

TABLE I. Sites of atoms demonstrating the considered graphs as a function of graph spacing constant λ.

Graph	Positions		
$\mathbb{P}_4$	**1:** $(-\lambda, 0, 0)$	**2:** $\left(-\frac{1}{2}\lambda, \frac{\sqrt{3}}{2}\lambda, 0\right)$	**3:** $\left(\frac{1}{2}\lambda, \frac{\sqrt{3}}{2}\lambda, 0\right)$
[Fig. 1(a)]	**4:** $(\lambda, 0, 0)$		
three-fan	**1:** $(0, 0, 0)$	**2:** $(-\lambda, 0, 0)$	**3:** $\left(-\frac{1}{2}\lambda, \frac{\sqrt{3}}{2}\lambda, 0\right)$
[Fig. 1(a)]	**4:** $\left(\frac{1}{2}\lambda, \frac{\sqrt{3}}{2}\lambda, 0\right)$	**5:** $(\lambda, 0, 0)$	
three-pan	**1:** $\left(\frac{-\lambda}{\sqrt{2}}, \frac{\lambda}{\sqrt{2}}, 0\right)$	**2:** $\left(\frac{-\lambda}{\sqrt{2}}, \frac{-\lambda}{\sqrt{2}}, 0\right)$	**3:** $(0, 0, 0)$
[Fig. 1(a)]	**4:** $(\lambda, 0, 0)$		
five-pan (W_1)	**5:** $\left(-\frac{1}{\sqrt{2}}\lambda - \frac{1}{2}\lambda\sqrt{1+2\sqrt{2}}, \frac{1}{2}\lambda, 0\right)$	**6:** $\left(-\frac{1}{\sqrt{2}}\lambda - \frac{1}{2}\lambda\sqrt{1+2\sqrt{2}}, -\frac{1}{2}\lambda, 0\right)$	
[Fig. 8(c)]			
seven-pan (W_2)	**5:** $\left(-\frac{1}{\sqrt{2}}\lambda - \lambda, \frac{1}{\sqrt{2}}\lambda, 0\right)$	**6:** $\left(-\frac{1}{\sqrt{2}}\lambda - \lambda, -\frac{1}{\sqrt{2}}\lambda, 0\right)$	
[Fig. 8(c)]	**7:** $\left(-\frac{1}{2}(2+\sqrt{2}+\sqrt{1+2\sqrt{2}})\lambda, \frac{1}{2}\lambda, 0\right)$	**8:** $\left(-\frac{1}{2}(2+\sqrt{2}+\sqrt{1+2\sqrt{2}})\lambda, -\frac{1}{2}\lambda, 0\right)$	
tower	**1:** $(0, 0, 0)$	**2:** $(0, -\lambda, 0)$	**3:** $\left(\frac{-\lambda}{\sqrt{2}}\frac{-\lambda}{\sqrt{2}} - \lambda, 0\right)$
[Fig. 1(a)]	**4:** $\left(\frac{\lambda}{\sqrt{2}}, \frac{-\lambda}{\sqrt{2}} - \lambda, 0\right)$	**5:** $\left(\frac{2\lambda}{\sqrt{2}}, \frac{-2\lambda}{\sqrt{2}} - \lambda, 0\right)$	**6:** $\left(0, -\lambda(1+\sqrt{2}), 0\right)$
	7: $\left(\frac{-2\lambda}{\sqrt{2}}, \frac{-2\lambda}{\sqrt{2}} - \lambda, 0\right)$		
$J_{14}/\bar{X}_{152}$	**1:** $(x_0, y_0, \eta_0\lambda)$	**2:** $\left(x_0, y_0 + \frac{\lambda}{\sqrt{3}}, -\lambda\right)$	**3:** $\left(x_0 - \frac{\lambda}{2}, y_0 - \frac{\lambda}{2\sqrt{3}}, -\lambda\right)$
[Fig. 7(a)]	**4:** $\left(x_0 + \frac{\lambda}{2}, y_0 - \frac{\lambda}{2\sqrt{3}}, -\lambda\right)$	**5:** $\left(x_0 + \frac{\lambda}{2}, y_0 - \frac{\lambda}{2\sqrt{3}}, -2\lambda * q_0\right)$	**6:** $\left(x_0, y_0 + \frac{\lambda}{\sqrt{3}}, -2\lambda * q_0\right)$
	7: $\left(x_0 - \frac{\lambda}{2}, y_0 - \frac{\lambda}{2\sqrt{3}}, -2\lambda * q_0\right)$	**8:** $(x_0, y_0, -\lambda(\eta_0 + 2q_0 + 1))$	
	where x_0 and y_0 are arbitrary points.		
	In calculations, we considered $x_0 = y_0 = 0$.		
	To get equal lengths of triangle and square		
	sides, we set $\eta_0 \simeq -0.183\,368$ and $q_0 = 1$.		

MWIS, or other optimization problems. These approaches can be implemented on a physical platform of ultracold neutral atoms using advantages provided by specific properties of laser-driven atomic systems with Rydberg interactions [6]. The first one is a quantum approximate optimization algorithm (QAOA) [7–9] and its hybrid quantum iterative version [10,11]. QuEra's quantum hardware processor Aquila has been used to find a solution for the max-cut problem and the IEEE 9-bus power grid graph state [12]. To physically implement the QAOA with neutral atoms, it is possible to use Rydberg excitation of the atomic ensemble by resonant laser pulses with varied pulse phases and durations. These variational parameters are used to generate the desired many-body evolution. The other approach is a variational quantum adiabatic algorithm (VQAA), which was theoretically proposed in [13], optimized for adiabatic paths in [14], and physically implemented with atomic ensemble in Refs. [15–17]. In this approach the detuning of a laser pulse exciting the atom to the Rydberg state is swept from the initial negative value to a large final positive value while the Rabi frequency is kept constant. The VQAA has shown better performance compared with the QAOA due to the difficulty of finding the optimal parameters for implementing the QAOA with high depth circuits [18]. A comparison of the performance of the state-of-the-art classical solvers with the QAOA and VQAA for different optimization problems has been reported [19,20]. Recently, many researchers have proposed hybrid methods and algorithms for using neutral-atom architectures to find solutions of graph problems [21,22]. A protocol for solving hard combinatorial graph problems by combining variational analog quantum computing and machine learning is assessed by quality score in Ref. [21]. Moreover, in Ref. [22] a hybrid digital-analog algorithm on Rydberg atoms shows the feasibility of the VQAA to the near-term implementation of quantum learning with the scalable architecture of arrays of neutral atoms.

Finding solutions for optimization problems as the MIS or MWIS of unit-disk graphs is beneficial for practical applications such as network design, scheduling tasks [23,24], gene selection, and prediction of protein-protein interaction in bioinformatics [25]. Realizing the solutions of the MIS has been experimentally achieved using an atomic architecture with quantum wires for planar and nonplanar graphs [3], transforming Platonic three-dimensional (3D) planar graphs to 2D planar graphs [26], using 3D spatial arrangements of atoms to embed non-unit-disk, nonplanar, or other more complex classes of graphs [27] and also for a large-size graph on the king's lattice [28]. Construction of rigorous and challenging solutions for the MIS problem via the adiabatic approach was presented in Ref. [29]. The framework for solving combinatorial optimization problems for non-unit-disk graphs was provided for MIS and max-cut problems in Ref. [30] and adjusting local detunings on atoms to approximate the MIS was studied in Ref. [31]. A generalized framework for solving the MWIS and other optimization problems was discussed in Refs. [32,33].

In this paper we study theoretically the problem of finding the MIS or MWIS on unit-disk graphs using an array of ultracold neutral atoms and the VQAA. We propose a nonlinear quasiadiabatic profile of sweeping the detuning from resonance when exciting atoms into Rydberg states. We study the quantum phases of matter by analyzing commensurate $\mathbb{Z}_n$-ordered states and incommensurate phases of matter in 1D and 2D spatial arrangements of atoms and we discuss the ability to construct a desired phase by controlling the system parameters. We study the effect of the sweeping rate on the generation of $\mathbb{Z}_n$-ordered states and the detection of domain walls and we calculate the critical detuning which is related to the minimum weight of each vertex in weighted graphs.

We investigate the solutions of the MIS and MWIS for planar and nonplanar graphs. Then we consider a dual-species quantum architecture for mediating the interaction between distant atoms by a quantum wire composed of atoms from different chemical elements. Quantum wires also can be used to consider non-unit-disk graphs. Dual-species quantum architectures are advantageous to avoid crosstalk between the graph atoms and wire atoms during the measurement process, following the initial proposal [34]. This architecture also provides opportunities for blockade enhancement and additional flexibility of interaction energies by dual-species Förster resonances. Moreover, we investigate the cost of employing quantum wires of different lengths on mediating the interaction between distant atoms for finding the MWIS.

The paper is organized as follows. In Sec. II we discuss the Hamiltonian of the atomic system and the procedure used for annealing the system to the desired many-body ground state. We show the dynamics of the states of a laser-driven single atom and of a spatially arranged ensemble of atoms representing a graph. In Sec. III we study the quantum phase transition of commensurate and incommensurate phases and discuss the ability to realize a floating incommensurate phase. In Sec. IV we discuss the results of MISs and MWISs for our simulation for planar graphs. In Sec. V we find the MISs and MWISs of a nonplanar graph representing a Johnson solid J_{14}, whose facets are different regular polygons in a three-dimensional array. The use of a heteronuclear quantum wire to mediate the interaction between distant atoms is discussed in Sec. VI. We summarize and discuss our results in Sec. VII.

II. QUANTUM SYSTEM

The spatially arranged array of atoms excited into the Rydberg states can be represented by a mathematical graph $G(V, E)$ in which the vertices V represent the atoms and the edges E represent the pairwise interaction between atoms. The governing Hamiltonian of this system can be written as

$$\hat{\mathcal{H}} = \hat{\mathcal{H}}_q + \hat{\mathcal{H}}_c, \tag{1}$$

where $\hat{\mathcal{H}}_q$ is the quantum driver Hamiltonian, which is composed of off-diagonal operators, and $\hat{\mathcal{H}}_c$ is the cost Hamiltonian [35,36]. Minimizing the cost parameters is an ultimate goal. The scheme of atomic energy levels is shown in Fig. 1(b). These two basic ingredients of the system Hamiltonian are given by

$$\hat{\mathcal{H}}_q = \frac{1}{2}\sum_{i}^{V}[\Omega(t)|g\rangle_i\langle r| + \text{H.c.}], \tag{2}$$

$$\hat{\mathcal{H}}_c = -\sum_{i}^{V}\Delta_i(t)\hat{n}_i + \sum_{i<j}^{E}\frac{\mathcal{C}_6}{|R_i - R_j|^6}\hat{n}_i\hat{n}_j, \tag{3}$$

where $|g\rangle = |5S_{1/2}, F = 2\rangle$ is the ground state of the trapped ^{87}Rb atom, $|r\rangle = |81S_{1/2}, m_j = 1/2\rangle$ is the Rydberg state, and the operator $\hat{n}_i = |r\rangle_i\langle r|$ is the projector to the Rydberg state of the ith atom. In addition, $\Omega(t)$ is a time-dependent effective two-photon Rabi frequency for the $|g\rangle \to |r\rangle$ transition with the maximum value $\Omega_0 = \Omega_{420}\,\Omega_{1013}/2\Delta_m$, where $\Omega_{420}/2\pi = 40$ MHz and $\Omega_{1013}/2\pi = 50$ MHz are the one-photon Rabi frequencies of laser radiation which couples $|g\rangle$ to $|r\rangle$ through the intermediate state $|m\rangle = |6P_{3/2}, F = 2, m_F = 2\rangle$, and $\Delta_m/2\pi = 570$ MHz is the detuning from the intermediate state. The values of Rabi frequencies are chosen to excite a single atom to the Rydberg state according to the considered timescale with high fidelity. Further, $\Delta_i(t)$ is the detuning from the two-photon resonance with the Rydberg state $|r\rangle$ of the atom or vertex i. For the MIS problem we set identical detunings for all atoms $\Delta_i(t) \equiv \Delta(t)$. Later, for the MWIS problem we will select detuning for each atom individually. We used the following shapes of time profiles $\Omega(t)$ and $\Delta(t)$ [see Fig. 1(c)]:

$$\Omega(t) = \begin{cases} \Omega_0\left(\frac{t}{t_{f_1}}\right), & 0 \leqslant t \leqslant t_{f_1} \\ \Omega_0, & t_{f_1} < t \leqslant t_{f_2} \\ \Omega_0 \frac{(t-\tau)}{(t_{f_2}-\tau)}, & t_{f_2} < t \leqslant \tau, \end{cases} \tag{4}$$

$$\Delta(t) = \begin{cases} \Delta_0, & 0 \leqslant t < t_{f_1} \\ \mathbb{A}\sin^2\left(\alpha_d \frac{t-t_{f_1}}{\tau}\right) + \Delta_0, & t_{f_1} \leqslant t < t_{f_2} \\ \Delta_f, & t_{f_2} \leqslant t \leqslant \tau. \end{cases} \tag{5}$$

Here $\tau = 5$ μs is a quantum annealing time, $t_{f_1} = \frac{1}{10}\tau$, and $t_{f_2} = \frac{9}{10}\tau$. In addition, Δ_0 and Δ_f are the initial and final values of Rydberg detuning. The amplitude $\mathbb{A} = (\Delta_f - \Delta_0)\csc^2(\alpha_d \frac{t_{f_2}-t_{f_1}}{\tau})$ guarantees that Δ will not exceed the predefined maximum of Δ_f for any possible value of the parameter $\alpha_d > 0$, which controls the course of detuning [see Fig. 1(c)]. The nonlinear quasiadiabatic time profile of the detuning at a constant value of Rabi frequency Ω_0 minimizes nonadiabatic excitations [37]; almost the same profile was used in [38] as the parameter of adiabatic path, which minimizes the cost Hamiltonian. To find the MISs of graphs with unweighted vertices, the value of Δ_f is kept constant. However, for graphs with weighted vertices the maximum value of the Rydberg state detuning Δ_f will define each vertex weight of the corresponding atom and should be selected individually for each atom, as we discuss later in Sec. IV B.

In the regime of the Rydberg blockade [39], when simultaneous laser excitation of two Rydberg atoms located at small interatomic distances becomes impossible, Rydberg interactions within an atomic array result in complex phases and phase transitions. For 1D arrays of interacting atoms the phase of a quantum system can be structured into $\mathbb{Z}_n$-ordered states ($n \geqslant 2$ is the number of sites separating neighboring Rydberg atoms), which are a class of commensurate phases. Spatial arrangements of Rydberg excitations in different 1D atomic arrays for the quantum phase of matter with commensurate order $\mathbb{Z}_2$, $\mathbb{Z}_3$, and $\mathbb{Z}_4$ and other possible incommensurate floating phases between $\mathbb{Z}_3$ and $\mathbb{Z}_4$ are shown in Fig. 1(d). The commensurate phases $\mathbb{Z}_2$ and $\mathbb{Z}_3$, numerically calculated for a 1D array of 10×1 atoms, are shown in Figs. 1(e), 1(f), and 1(g), respectively. The details of the numeric calculations will be given below.

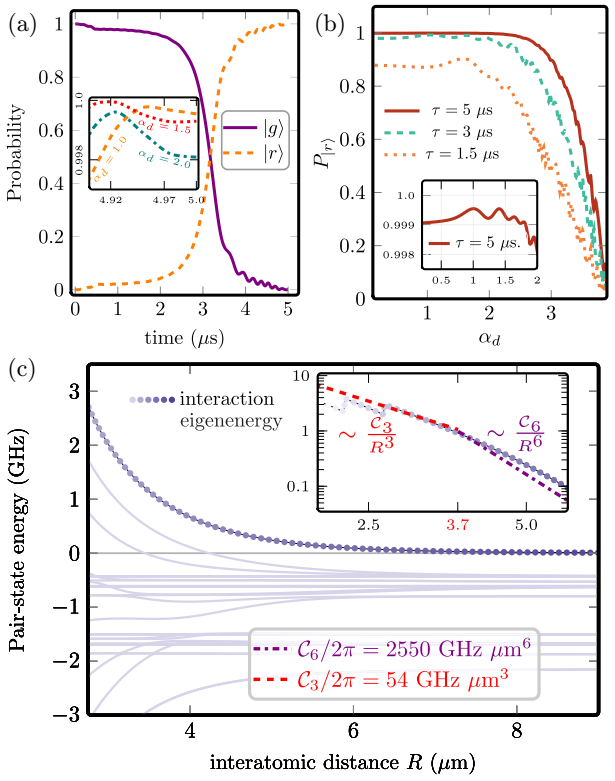

FIG. 2. (a) Time dynamics of the probabilities of ground and Rydberg states during Rydberg excitation of a single atom for different values of α_d. (b) Probability of exciting a single atom to the Rydberg state $P_{|r\rangle}$ as a function of the detuning course parameter α_d for different values of annealing time τ. (c) Pair-state interaction energy for two ^{87}Rb, $|81S_{1/2}, m_j = 1/2\rangle$ Rydberg atoms. Teal solid curves are the eigenenergies of the interaction matrix after diagonalization, calculated using the alkali Rydberg calculator [40], with $\theta = 0$, $\phi = 0$, $\delta n = 2$, and $\delta l = 1$. Curves are the fitting approximations for short-range dipole-dipole (red dashed curve) and long-range van der Waals (violet dash-dotted curve) regimes, showing that $\mathcal{C}_3/2\pi = 54\,\text{GHz}\,\mu\text{m}^3$, $\mathcal{C}_6/2\pi = 2550\,\text{GHz}\,\mu\text{m}^6$, $R_\text{L} = 2.0\,\mu\text{m}$, and $R_\text{vdW} = 3.7\,\mu\text{m}$. The inset shows a log-log plot of the fitting values and the corresponding eigenenergy.

The numerically calculated probabilities to excite a single atom to the Rydberg state using the quasiadiabatic profile from Eq. (5) are shown in Fig. 2(a) with a probability of 0.9995 for the Rydberg state $|r\rangle$. Here, for simplicity, we neglect spontaneous decay of the excited states, and the fidelity is limited purely by the nonadiabatic dynamics of the quantum system. The inset in Fig. 2(a) shows the effect of different courses α_d of sweeping the detuning on the calculated probability of the single-atom Rydberg excitation. In Fig. 2(b) we plot the probability of exciting a single atom to the Rydberg state as a function of the detuning course parameter α_d for different annealing times. We choose $\alpha_d = 1$ in our calculations, since it provides the maximum excitation probability, as shown in the insets of Figs. 2(a) and 2(b).

For any two vertices i, j ($i \neq j$) on a graph, which are represented by two atoms separated by an edge E, defined by

interatomic distance $R = |R_i - R_j|$, the interaction between atoms can be either a short-range dipole-dipole interaction of approximately C_3/R^3 for $R < R_{\rm vdW}$ or a long-range van der Waals (vdW) interaction of approximately C_6/R^6 for $R_{\rm vdW} < R$. The interatomic distance should be much larger than the Leroy radius $R_{\rm L}$, which marks the minimum interatomic distance between two atoms to satisfy Leroy-Bernstein theory [41]. The vdW radius $R_{\rm vdW}$ characterizes the border between different interaction regimes. It depends on the structure and properties of the atomic energy levels of a particular chemical element and can be significantly increased in cases of an asymmetric homonuclear or heteronuclear Rydberg interaction in the vicinity of Förster resonances [34,42]. In Fig. 2(c) we show the eigenenergies of the interaction Hamiltonian for two atoms excited symmetrically to the Rydberg state $|81S_{1/2}, m_j = 1/2\rangle$. We use the alkali Rydberg calculator [40] for calculations. The dominant regime for interatomic distances $R > R_{\rm vdW} = 3.7\,\mu$m is the vdW interaction with $C_6/2\pi = 2550\,\text{GHz}\,\mu\text{m}^6$. The Rydberg blockade occurs when $R < R_b = (C_6/\Omega_0)^{1/6}$, where R_b is a blockade radius.

We use a time-dependent Schrödinger equation $i\hbar\frac{\partial}{\partial t}|\psi\rangle = \hat{\mathcal{H}}|\psi\rangle$ to calculate the time dependences of probabilities in Fig. 1(c) for any graph with $N \geqslant 8$ vertices and to plot the phase diagrams of $\mathbb{P}_4$ and seven-pan graphs in Figs. 1(a), and 8(d), respectively. We perform a Monte Carlo simulation with the Lindblad master equation considering the radial positional fluctuations $\delta_R = \sqrt{\delta_x^2 + \delta_y^2}$ of each atom arising from fluctuations in trapping power. Also, the axial positional fluctuations δ_z arising from the nonzero temperature of trapped atoms are considered in the calculations. The Lindblad master equation is written as

$$\frac{d}{dt}\hat{\rho} = -\frac{i}{\hbar}[\hat{\mathcal{H}}, \hat{\rho}] + \sum_i^V \left(\hat{L}_i\hat{\rho}\hat{L}_i^\dagger - \frac{1}{2}\{\hat{L}_i^\dagger\hat{L}_i, \hat{\rho}\}\right), \quad (6)$$

where $\hat{\rho}$ is the density matrix and $\hat{L}_i = \sqrt{\frac{1}{2}\gamma_m}\hat{n}_i$ is the jumping operator describing the dissipative processes in the system, with $\gamma_m = 1/\tau_{|m\rangle}$ the decay of the intermediate state $|m\rangle$ with lifetime $\tau_{|m\rangle} = 0.118\,\mu$s.

III. QUANTUM PHASE TRANSITIONS

The solution for the MIS and MWIS for unit-disk graphs can be found in the ordered phases of $\mathbb{Z}_2$ or $\mathbb{Z}_3$, depending on the spatial arrangement of the graph vertices. In this section we study the commensurate (or ordered) and incommensurate states for a linear arrangement of atoms, with the aim of obtaining a clear understanding of the regimes and stability of solutions.

In the atomic arrays, a quantum phase transition into the $\mathbb{Z}_n$-ordered state was realized experimentally in the 1D array [43,44], on a 1D ring [45], and on a 2D checkerboard phase [16], which enabled the investigation of the quantum Kibble-Zurek mechanism (QKZM) [46,47] and the critical dynamics of ordered states. The QKZM provides a solid understanding of the nonequilibrium dynamics of cosmological, particle, and condensed-matter systems [48]. Ordered states are beneficial for creating exotic states of matter with topological order, such as a quantum spin liquid [49]. The transition from the disordered phase to the ordered phase takes place at a specific value of the Rydberg detuning Δ_c depending on the phase of the transition and the value of the sweeping rate. Here Δ_c is called the critical detuning. The QKZM of commensurate phases of $\mathbb{Z}_n$-ordered states of an atomic array was studied earlier in Refs. [16,43–45,50] for equal maximum values of Rydberg detuning for all atoms in the array. Consequently, the value of critical detuning Δ_c is related to the number of separated sites n of $\mathbb{Z}_n$-ordered states. Therefore, the parameters of critical dynamics, such as critical length and critical scaling exponents, which characterize the Ising universality class and the QKZM, can be obtained. Also, critical incommensurate phases (floating phases) were theoretically predicted in a 1D Rydberg array [51–53] and experimentally observed in 2D ladder Rydberg arrays [54].

To keep the interaction between atoms in the vdW regime, we restrict our calculations to $1 \leqslant R_b/a \leqslant 3.2$. For this restriction we find that the realization of $\mathbb{Z}_4$ is not conceivable. In our numeric simulations of the commensurate phases $\mathbb{Z}_2$ and $\mathbb{Z}_3$ of the 1D array of 10×1 atoms, which are shown in Figs. 1(e)–1(g), we have four and three spins for $\mathbb{Z}_2$ and $\mathbb{Z}_3$, respectively. For the $\mathbb{Z}_2$-ordered state, the interruption of the ordering sequence is observed [which is indicated by the red rectangle in Fig. 1(e)]. This interruption of the ordering is called a domain wall, which occurs in different positions of the array. Domain walls are identified as having either one atom at the edge of the array in ground state or two neighboring atoms in the same state [43].

Figure 3 illustrates the effect of the sweeping rate v on the probability of finding the ordered state $\mathbb{Z}_2$. In an ideal case without domain walls, as shown in Fig. 3(a), it is clear that with increasing sweeping rate the maximum possible probability of the ordered state decreases. In Fig. 3(b) we plot the susceptibility $\chi = \partial\langle n\rangle/\partial\Delta_f$, which is calculated by interpolating the numerical data and then differentiation. The maximum value of the susceptibility corresponds to the critical value of detuning Δ_c. From Fig. 3(b) it is clear that with an increase of the sweeping rate the value of Δ_c/Ω_0 shifts to higher values. This is analogous to results of Ref. [45]. A pulse profile with moderate sweeping rate can minimize the detuning parameter in the cost Hamiltonian. To find a solution for the MWIS, in Sec. IV B we define the weight $w_i > \Delta_c$ of a vertex i. For quantum annealing time $\tau = 5\,\mu$s we select the weights following the condition $w_i > 0.8\,\Omega_0 = 2\pi \times 1.4\,$MHz and keep the lattice spacing constant at approximately $a \simeq \frac{1}{1.5}R_b$.

The construction of the $\mathbb{Z}_2$-ordered state with a defect (domain wall) induced by an ancilla and optimizing the driving fields on QuEra's quantum hardware Aquila was performed in Ref. [55]. The transition from the $\mathbb{Z}_2$-ordered to the $\mathbb{Z}_3$-ordered crystalline state occurs at $R_b \simeq 2a$. In our simulation, we find that the incommensurate phases between $\mathbb{Z}_2$ and $\mathbb{Z}_3$ for a 1D spatial arrangement do not exist, as concluded in [44], despite the fact that they were predicted in Ref. [56]. According to our calculations, in the range of validity of the vdW interaction, an incommensurate floating phase emerged in the regime of $2.6 \leqslant R_b/a \leqslant 3.2$ and $\Delta_f/\Omega_0 \geqslant 1$. This is supposed to be a floating phase between $\mathbb{Z}_3$ and $\mathbb{Z}_4$.

There are two types of domain walls depending on the number of interrupted sites [57]. Domain walls of type I and

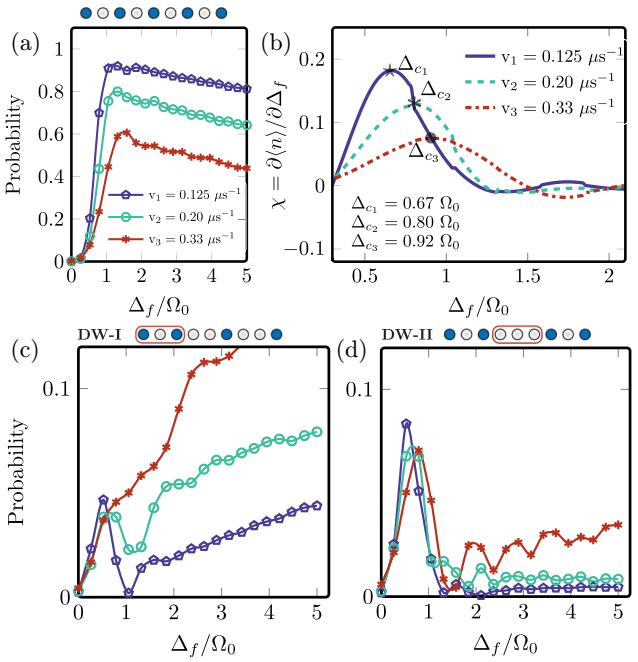

FIG. 3. (a) Probability of obtaining the ordered state $\mathbb{Z}_2$ for an array of 9×1 atoms as a function of the dimensionless parameter Δ_f/Ω_0 for different values of the annealing time τ by considering $R_b/a = 1.5\,\mu$m. (b) Susceptibility $\chi = \partial\langle n\rangle/\partial\Delta_f$ for different sweeping rates, showing the critical detuning Δ_c as the value of detuning corresponds to the maximum value of χ. Also shown is the probability of obtaining (c) the first and (d) the second type of domain wall in a $\mathbb{Z}_n$ chain of atoms.

type II include two and three interrupted sites, respectively. High sweep rates reduce the probability of obtaining an ideal case for the ordered state $\mathbb{Z}_2$, as illustrated in Fig. 3(a). Therefore, the possibility of obtaining a chain of atoms with interrupted sites, or domain walls, increases. In Figs. 3(c) and 3(d) we show the effect of increased sweeping rates on the probability of obtaining an interrupted $\mathbb{Z}_n$ state with type I and type II domain walls, respectively.

IV. PLANAR GRAPHS

A. Maximum independent set

The maximum independent sets of unweighted planar graphs are obtained for the maximum Rydberg detuning Δ_f equal for all atoms resembling the graph, as shown in Fig. 1(a). Here we omit the weights of the vertices. The graph spacing constant λ defines the distance between vertex i and the nearest vertex j ($i \neq j$) and is an alternative to the lattice constant a, which is shown in Fig. 1(d).

The phases of the $\mathbb{P}_4$ graph, shown in Fig. 1(a), could be different from the phases of an 1D atomic array due to differences in the energies of all pairwise interactions in a two-dimensional graph. In Fig. 4 the phase diagram of the $\mathbb{P}_4$ graph shows regions of dominant phases. The phase diagram is obtained by parametrizing the Hamiltonian via the ratios R_b/λ and Δ_f/Ω_0. The positions of the graph vertices are given in Table I as a function of the graph spacing constant λ. Fluctuations of positions of atoms, laser noise, and spontaneous

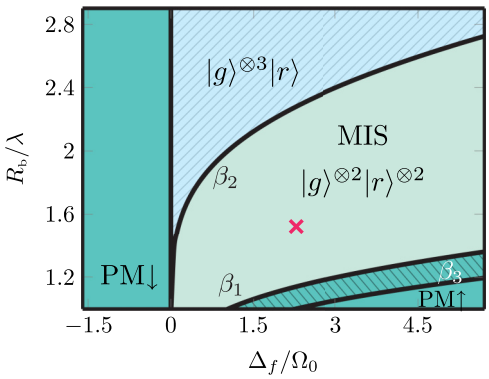

FIG. 4. Phase diagram of the $\mathbb{P}_4$ graph showing the regions of dominant phases. The antiferromagnetic phase where atoms are singly excited to the Rydberg state is bounded by $0 < \Delta_f/\Omega_0 \leqslant \beta_2(R_b/\lambda)$. The MIS phase is dominant in the region $\beta_1(R_b/\lambda) < \Delta_f/\Omega_0 < \beta_2(R_b/\lambda)$. There are two PM phases: (i) the PM↓ phase of ground states, which is bounded by $\Delta_f/\Omega_0 < 0$, and (ii) the PM↑ phase, which is bounded by $\Delta_f/\Omega_0 > \beta_1(R_b/\lambda)$. The phase bounded within $\beta_1(R_b/\lambda) < \Delta_f/\Omega_0 < \beta_3(R_b/\lambda)$ is where three atoms can be excited to the Rydberg state simultaneously.

emissions are neglected. The boundaries between different phases can be fitted by functions $\beta_i(\frac{R_b}{\lambda}) = \frac{1}{4}\mathcal{C}_6^{\text{Rb-Rb}} e^{-\xi_i R_b/\lambda}$,[1] where the parameters $\xi_1 = 1.4$, $\xi_2 = 2.8$, and $\xi_3 = 1.23$ define three different curves β_1, β_2, and β_3, shown in Fig. 4. There are two different regions where paramagnetic (PM) phases are dominant: (i) The PM↓ phase is located where $\Delta_f < 0$ and only the ground state of all four atoms $|g\rangle^{\otimes 4}$ can be found in this region of parameters and (ii) the PM↑ phase is located where $\Delta_f/\Omega_0 > \beta_3$, where all atoms are excited to the Rydberg state. The bounded phase within $\beta_3 \leqslant \Delta_f/\Omega_0 \leqslant \beta_1$ is a PM↑-like phase where three atoms can be excited to the Rydberg state. For $0 < \Delta_f/\Omega_0 \leqslant \beta_2$, we observe a phase with only one atom excited to the Rydberg state due to the strong interaction between atoms. The state of the system in this phase can be written as $|\psi\rangle = \sum_{l\neq i,j,k}^{N} |g\rangle_{i,j,k}^{\otimes 3}|r\rangle_l$. The region bounded between β_1 and β_2 is an antiferromagnetic phase revealing the MISs.

In Fig. 5 we show the calculated probability distributions of all possible states of an atomic system after being driven to the many-body ground state. We set the values of the graph spacing constant $\lambda = 7.0\,\mu$m and the maximum value of Rydberg detuning $\Delta_f/\Omega_0 = 2.28$, which are compromised values for finding MISs, as pointed out in Fig. 4. These values of λ and Δ_f will be constant for all graphs in Fig. 5. We consider finite lifetimes of intermediate excited and Rydberg states using Lindblad equation and perform a Monte Carlo simulation to take into account fluctuations of atomic positions.

The MISs of the $\mathbb{P}_4$ graph are **{**$\{1, 3\}, \{1, 4\}, \{2, 4\}$**}**. These states are shown in Fig. 5(a) as positions of Rydberg atoms, i.e., state $\{1, 3\}$ corresponds to first and third atoms excited into Rydberg states. Their probabilities are represented by violet bars. From Fig. 5(a) we can see that the quantum states corresponding to solutions of the MIS demonstrate the

[1]We consider here the numerical value of $\mathcal{C}_6$.

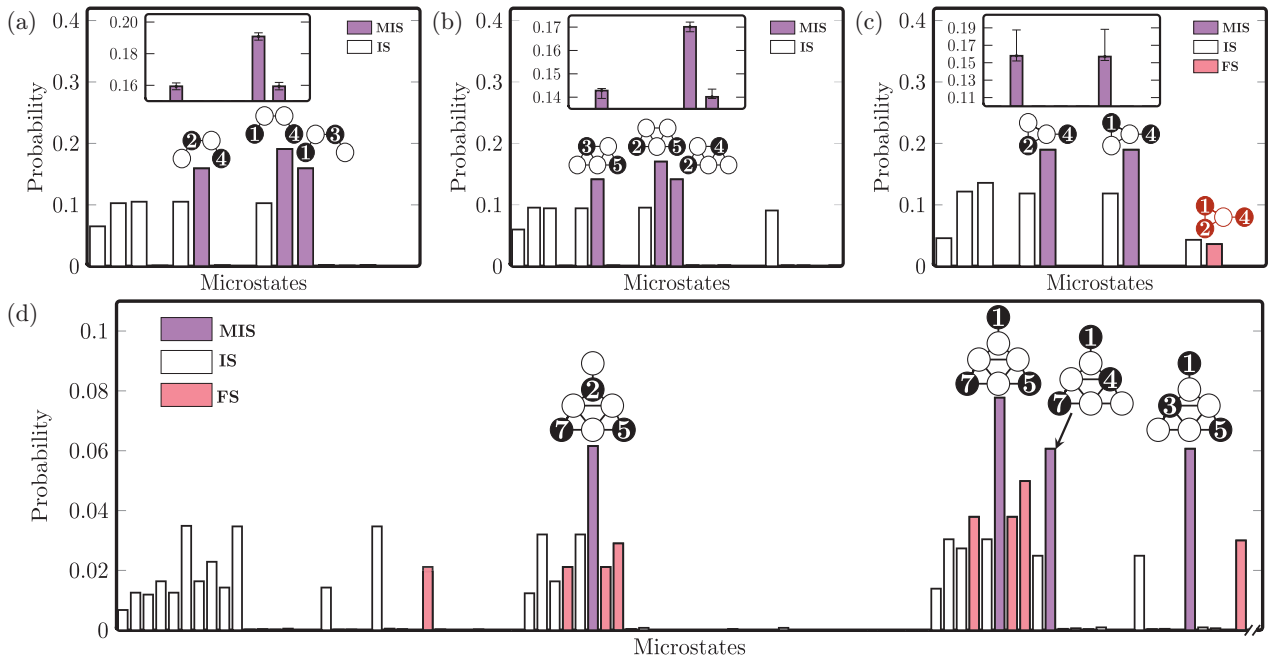

FIG. 5. Probability distributions indicating the MIS solutions (violet bars) of the graphs (a) $\mathbb{P}_4$, (b) three-fan, (c) three-pan, and (d) Eiffel-tower, for $\Delta_0/2\pi = -6.0\,\text{MHz}$, $\Delta_f/2\pi = 4.0\,\text{MHz}$, $\tau = 5.0\,\mu\text{s}$, and the graph spacing constant $\lambda = 6.0\,\mu\text{m}$. The insets show the errors bars resulting from considering positional (radial and axial) fluctuations $\delta_R = \pm 0.447\,\mu\text{m}$ ($\delta_x = \delta_y = 0.1\,\mu\text{m}$) and $\delta_z = \pm 0.6\,\mu\text{m}$. White (red) bars correspond to the independent sets (frustrated sets). In (d) only the first 90 states of a total of $2^7 = 128$ states are shown. The probabilities of other states are infinitely small. A black-filled circle indicates a weightless vertex whose corresponding atom is excited to the Rydberg state with labels indicating the vertex number. Open circles correspond to atoms in the ground state.

highest probabilities. Finding the MISs of unit-disk graphs is a geometry-constrained problem, and the probabilities of MISs can be varied by adjusting the distance between vertices according to the phase diagram. The MISs of a three-fan graph, shown in Fig. 5(b), are the same as in the $\mathbb{P}_4$ graph, since vertex 1 is connected to all other vertices. However, the probabilities of MISs in the three-fan graph are lower than the corresponding probabilities of MISs in the $\mathbb{P}_4$ graph. The sets $\{1, 3\}$ and $\{2, 4\}$ of $\mathbb{P}_4$ and $\{2, 4\}$ and $\{3, 5\}$ of the three-fan graph are of the same geometric pattern and consequently have the same probabilities. The error bars in the inset show the range of calculated errors for the MIS states (plotted in the same sequence as in the main figure) due to the fluctuations of the atomic positions. The white bars show the probability of a single atom being excited to the Rydberg state, which corresponds to an independent set of the graph.

The MISs of the three-pan graph, shown in Fig. 5(c), are $\{\{1, 4\}, \{2, 4\}\}$. The corresponding states have almost equal probabilities, since both vertices 1and 2 are equally displaced from vertex 4. Also, the frustrated set or configuration $\{1, 2, 4\}$ appears in the calculations due to an imperfect Rydberg blockade for vertices 1 and 2.

Figure 5(d) shows the MISs of the Eiffel Tower graph [shown in Fig. 1(a)], which can be considered a combination of three-pan and three-fan graphs. The MISs of the tower graph are $\{\{1, 5, 7\}, \{1, 3, 5\}, \{1, 4, 7\}, \{2, 5, 7\}\}$. Frustrated configurations are also present, but they have lower probabilities than those of the MISs. The MISs $\{\{1, 3, 5\}, \{1, 4, 7\}\}$ have identical geometric patterns and their probabilities are almost equal.

B. Maximum-weight independent set

In this section we study the MWIS of the same graphs, which are shown in Fig. 1(a), but take into account the weights of their vertices. The positions of the vertices and weights are defined in Table I and the weights are indicated in Fig. 1(a). The goal of the MWIS is to find the independent set with the maximum sum of its weights. The weight of each vertex is represented by the maximum value of Rydberg detuning Δ_f [58]. The weights Δ_f of vertices are not equal. Therefore, the probability of exciting a particular atom to the Rydberg state is different. In Fig. 6 we show the calculated probabilities of transition of the atomic ensemble from the ground state $|g\rangle^{\otimes N}$ to many-body states with a different configuration of Rydberg excitations. In Fig. 6(a) the MWIS of the $\mathbb{P}_4$ graph is the set $\{1, 3\}$, which has a much higher probability than other independent sets. Also, it can be noted that the probability of state $\{2, 4\}$ is higher than that for $\{1, 4\}$, which is different from the results in Fig. 5(a) for the MIS problem. Analogous results are obtained in Fig. 6(b). The MWIS for the three-pan graph in Fig. 6(c) is $\{1, 4\}$. It worth noting that the calculated probability for the frustrated set $\{1, 2, 4\}$ is much higher than obtained before for the MIS problem for the same graph in Fig. 5(c).

Overall, we note here that the MWIS problem is not only a geometry-constrained one as in the MIS. The probabilities

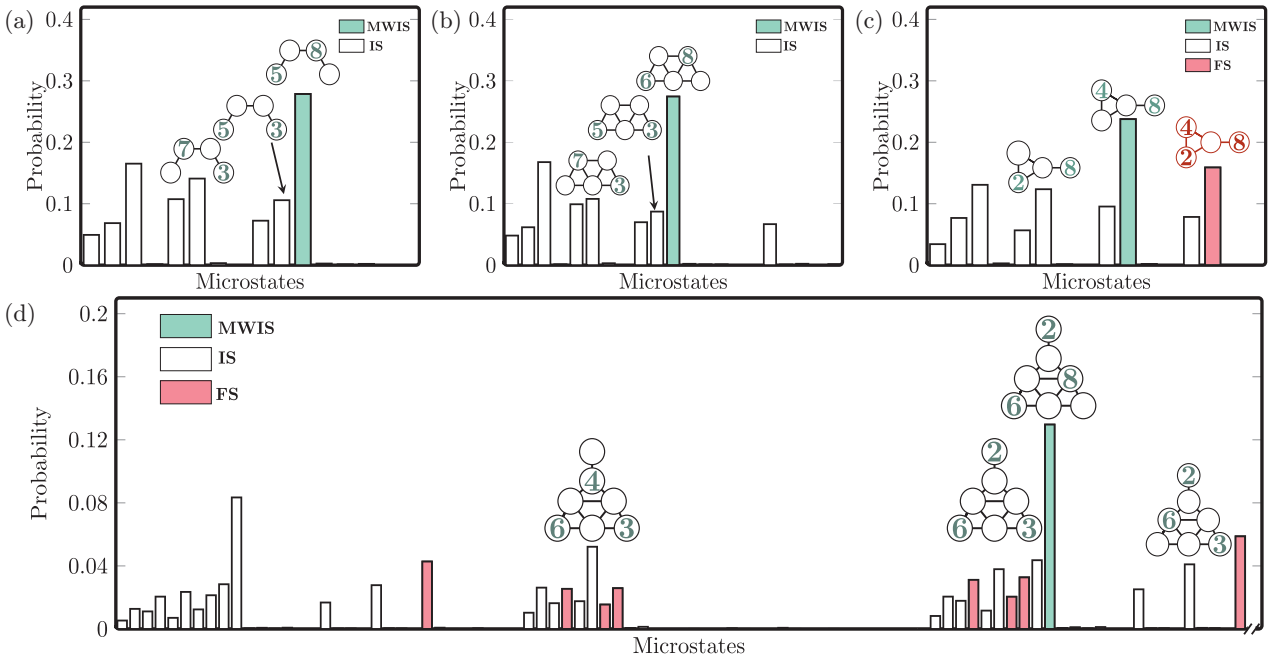

FIG. 6. Probability distributions indicating the MWIS solutions (green bars) of the corresponding graphs in Fig. 1(a) with the same values of parameters as in Fig. 5 but with different values of Δ_f (see the text for details). White (red) bars correspond to the independent sets (frustrated sets). A circle with a number indicates that the corresponding atom is excited to the Rydberg state, with the light green label indicating the weight of this vertex and the open circles representing atoms in the ground state.

of independent sets with the same geometric pattern are not equal. Also, the probabilities of the MISs are sorted in ascending order of the sum of their weights.

V. NONPLANAR GRAPH

In this section we discuss the results of finding the MWIS and MIS of a nonplanar graph. Figure 7(a) shows a 2D scheme representation of the J_{14} graph. The J_{14} is a graph with eight vertices in three dimensions, as defined in Table I. The J_{14} graph is known as an elongated equilateral triangular bipyramid, which is one of Johnson's 92 convex polyhedra solids [59], whose facets are regular polygons. The graph includes $\mathcal{F} = 9$ faces, as six equilateral triangles and three squares. Euler's characteristic of this graph is $\chi = V - E + \mathcal{F} = 2$. A similar nonplanar graph, represented in two dimensions, is called $\bar{X}_{152}$, as classified in the nomenclature of the Information System on Graph Classes and their Inclusions [60]. The J_{14} graph is a combination of two three-pan graphs.

In Fig. 7(b) we plot the calculated probabilities of MISs and MWISs for the J_{14} graph in two cases. In the first case all vertices are equally weighted, which shows the MISs $\{\{1,5\},\{1,6\},\{1,7\},\{1,8\},\{2,8\},\{3,8\},\{4,8\}\}$ in violet-colored bars. The sets $\{\{1,5\},\{1,6\},\{1,7\},\{2,8\},\{3,8\},\{4,8\}\}$ have the same probability due to the fact that the atoms, representing vertices, are physically displaced equally from each other. Frustrated sets can be obtained from the simulation with probabilities much smaller than those of the MISs. In the second case the weights of vertices are not equal [the weight of each vertex is labeled in green in Fig. 7(a)]. The MWIS according to the considered weights is $\{1,5\}$, as shown by a green bar in Fig. 7(b). The independent sets, when considering the weighted graph, are the over plotted black bars. The frustrated set $\{1,2,\ldots,8\}$ ($|r\rangle^{\otimes 8}$) is shown by the red bar and exhibits infinitely low probability.

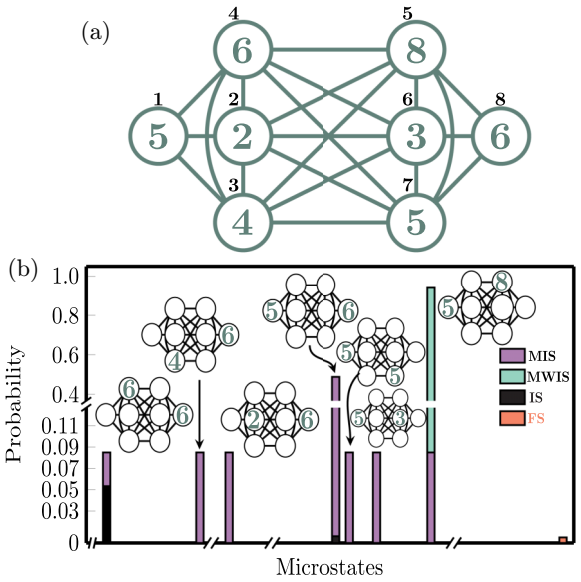

FIG. 7. (a) 2D representation of the scheme of the Johnson solid J_{14} graph. The black label is the vertex number and the green label represents the weight of each vertex. The exact positions of the vertices are given in Table I. (b) Probabilities of MWISs for J_{14}. Some of the graph states with infinitely small probabilities are omitted from the plot.

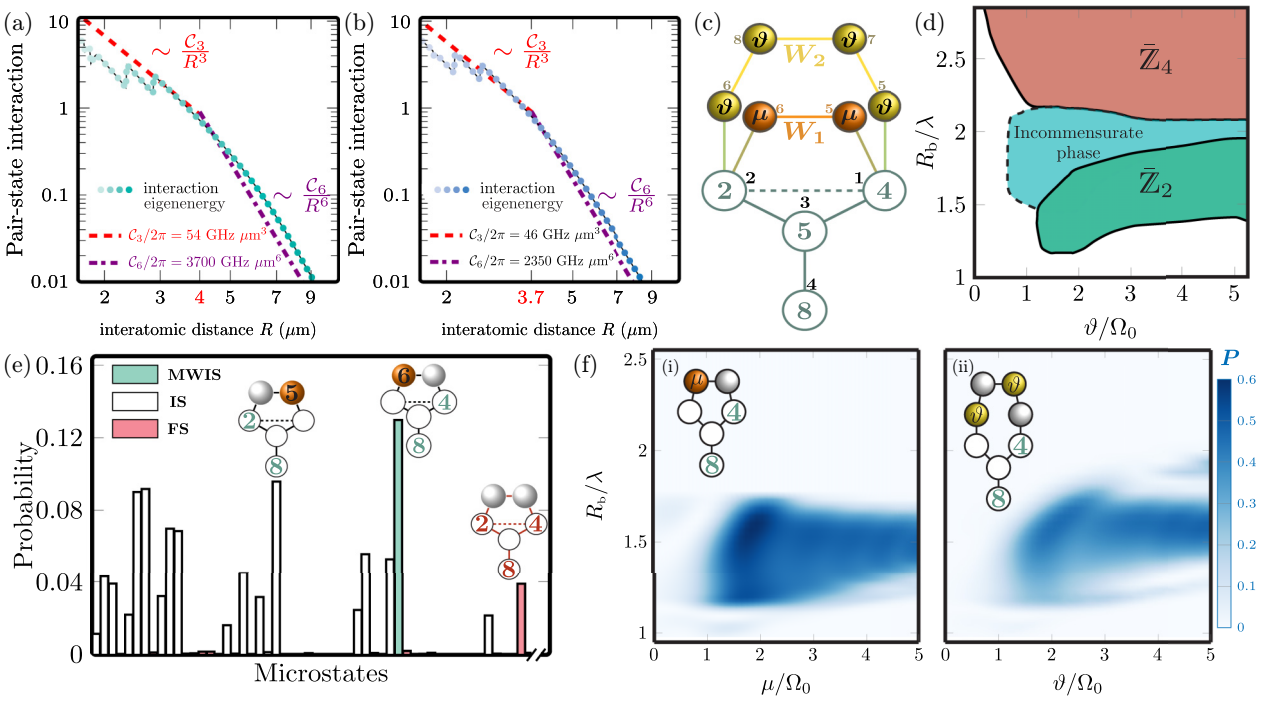

FIG. 8. (a) Pair-state energy (GHz) for the heteronuclear interaction between Rb and Cs atoms excited simultaneously to the Rydberg state $|81S_{1/2}, m_j = 1/2\rangle$ considering the same conditions and methods in Fig. 1(c). (b) Pair-state energy interaction energy between two Cs atoms. (c) Graph scheme of the three-pan graph with vertices 1 and 2 connected using two different spatial configurations of quantum wires W_1 (two vertices in violet) and W_2 (four vertices in orange). (d) Phase diagram of the mediation of the vertices v_1 and v_2 by the quantum wire W_2, which is composed of four equally weighted vertices (weight ϑ MHz). (e) Probabilities indicating the MWIS of the five-pan graph (3-pan+W_1). (f) Contour plots of the probability **P** of the MWIS of (i) the five-pan graph and (ii) the seven-pan graph as a function of dimensionless parameters μ/Ω_0 (ϑ/Ω_0) and R_b/λ.

VI. QUANTUM WIRE

In this section we consider mediating a strong interaction between distant vertices using the concept of a quantum wire [3,61]. Here we consider a dual-species quantum architecture by considering the wire to be composed of atoms from a different alkali-metal element used for graph representation. The dual-species architecture allows separation of the readout wavelengths during detection of the MIS or MWIS and suppression of crosstalk between neighboring atoms. The heteronuclear Rydberg interaction in atomic arrays was first discussed in Ref. [34]. The concept of dual-species quantum annealers was then introduced in Ref. [4]. A dual-species heteronuclear Rb-Cs array of ultracold atoms was experimentally demonstrated in Ref. [62]. Schemes of controlled-NOT gates with several control and target atoms exploiting heteronuclear Rydberg interactions were studied in Ref. [42]. The two-qubit controlled-Z gate with different chemical elements was demonstrated in Ref. [63], showing advantages compared with single-species homonuclear architectures. The scalability of heteronuclear atomic architecture with coherent transport of control qubits was studied in Ref. [64]. Analysis of heteronuclear interspecies interactions between Rydberg d states of Rb and Cs atoms was presented in Ref. [65]. A dual-element model of quantum processors with single atoms or superatoms in the regime of Rydberg blockade was developed for quantum computations without the need of local addressing [66]. Here we propose using a quantum wire of Cs atoms created from an array of traps generated by an acousto-optic deflector, with the graph represented by Rb atoms, which are loaded in the array of static traps generated by a spatial light modulator. The ground state of Cs atoms of the quantum wire $|g\rangle_W = |6S_{1/2}, F = 3, m_F = 3\rangle$ are excited to the Rydberg state $|r\rangle_W = |81S_{1/2}, m_j = 1/2\rangle$ through the intermediate state $|m\rangle_W = |7P_{3/2}, F = 2\rangle$ by using 460- and 1039-nm laser lights, respectively. Atoms representing the graph and the wire are excited to the Rydberg state with the same principal quantum number $n = 81$. In this case the dominant regime of interaction is the van der Waals regime [39]. Figures 8(a) and 8(b) show the interaction between pairs of Rb and Cs atoms (graph and wire) and pairs of Cs atoms (wire and wire), respectively. For an interatomic distance $R > R_{vdW} \simeq 4\,\mu$m, it is guaranteed that all interactions are in the vdW regime. The values of $\mathcal{C}_3$ and $\mathcal{C}_6$ for all interactions are calculated by fitting the curves with the calculated interaction energy with all the parameters as in Fig. 2(c). The quantum wire should be in the antiferromagnetic phase, where at most only one of the adjacent atoms can be excited to the Rydberg state, known as the $\mathbb{Z}_2$ phase.

Figure 8(c) illustrates mediation of the interaction between the vertices v_1 and v_2 of a three-pan graph by two quantum wires W_1 and W_2 formed by Cs atoms. The quantum wires are of different lengths (have different numbers of atoms) $\bar{w}_1 = 2$ and $\bar{w}_2 = 4$. Atoms of each wire are equally weighted. The weights of the quantum wires are $\mu/2\pi$ for W_1 and $\vartheta/2\pi$ for W_2.

In Fig. 8(d) we plot the phase diagram of a three-pan graph with quantum wire W_2 showing the probabilities as a function of two dimensionless parameters: the ratio of wire weights to the effective Rabi frequency ϑ/Ω_0 and the ratio of Rydberg blockade radius to the graph spacing constant R_b/λ [67]. In general, the obtained phase diagrams can vary for the same type of graph depending on the spatial arrangement of the atoms and the properties of the interactions between atoms. Hence, the discussion about phase diagrams here is valid only for the considered spatial arrangement of the atoms. If the quantum wire W_2, consisting of four atoms, is not connected to graph atoms, then the probability distribution of its quantum states for the same laser excitation pattern, as shown in Fig. 2(c), should behave similarly to the phase diagram, shown in Fig. 4. The phase diagram in Fig. 8(d) shows the realization of a different ordered state $\bar{\mathbb{Z}}_2$ [the bar sign over $\mathbb{Z}_2$ indicates that the ordered states for a graph are different from the linear configuration from Fig. 1(d)]. The ordered state $\bar{\mathbb{Z}}_4$ is also realized for the graph-wire states $|gggr\rangle_G|gggr\rangle_{W_2}$ and $|gggr\rangle_G|ggrg\rangle_{W_2}$.

In Fig. 8(e) we show the probabilities of finding the MWIS ($\{1,4\} = |rggr\rangle_G|gr\rangle_{W_1}$) of the three-pan graph while using the quantum wire W_1 to mediate the interaction between v_1 and v_2. Finding the MWIS $\{1,4\}$ of the three-pan graph is independent of the wire weights μ, as shown in Fig. 8(f), and the MWIS is $\{1,4,\mathbf{6}\}$ (the bold text indicating the wire atom excited to the Rydberg state). We plot the probabilities of states $\{1,4,\mathbf{6}\} = |rggr\rangle_G|gr\rangle_{W_1}$ and $\{1,4,\mathbf{6},\mathbf{7}\} = |rggr\rangle_G|grrg\rangle_{W_2}$ in Figs. 8(f i) and 8(f ii), respectively. The contour plot shows the probability of the considered state as a function of the weights of the wire atoms and distance parameter λ. In this figure we illustrate the effect of using quantum wires of different lengths (numbers of atoms). As shown, the minimum value of the vertex weight for the probability of the MWIS with a quantum wire W_1 formed by two auxiliary atoms is $\mu/\Omega_0 \simeq 0.92$ and for a quantum wire W_2 formed by four auxiliary atoms $\vartheta/\Omega_0 \simeq 1.2$. The slightly increased cost for employing different lengths of a quantum wire to mediate the distant atoms is due to the spatial arrangement of the wire and graph atoms, which is interrupted by undesirable weak interactions.

Due to the spatial arrangement of atoms representing the graph, an incommensurate phase emerges, showing a combination of $\bar{\mathbb{Z}}_2$- and $\bar{\mathbb{Z}}_3$-ordered states. The probability distribution of the incommensurate state is shown in Fig. 9. The realization of this incommensurate phase is controlled by the Rydberg detuning of each atom of the considered array in the 2D spatial arrangement of the atoms. This phase may boost realizing new dimer models which can be obtained from optimizing the interaction between atoms of homonuclear or heteronuclear architecture with the detuning of the Rydberg state of each atom. In Fig. 8(f) the length of the quantum wire changes the dynamics of the system. In this case the quantum wire is not in an antiferromagnetic phase and that breaks the considered condition [3]; then the quantum wire W_2 can be regarded as a superatom [66].

In terms of phases of MWIS solutions, using the longer wire W_2 to find the solution is quite different from using the shorter wire W_1. In W_1 the only phase for the solution

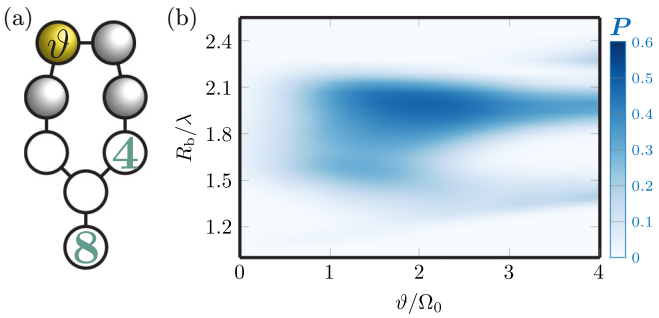

FIG. 9. Probability distribution **P** of the incommensurate state $|rggr\rangle_G|gggr\rangle_{W_2}$.

is the case when the sixth atom is excited to the Rydberg state, which blocks Rydberg excitation of the second and fifth atoms. At the same time, for the W_2 wire there are two phases, which is the case of Fig. 8(f ii) (the sixth and seventh atoms are excited to the Rydberg state) in addition to Fig. 9(b) (only the eighth atom is excited to the Rydberg state). Both phases can be shown as solutions. The case shown in Fig. 9(b) is a solution with $\Delta_f/\Omega_0 \geqslant 1$, but for a different range of interatomic distances compared with Fig. 8(f i).

VII. CONCLUSION

We proposed and optimized a quasiadiabatic profile for sweeping the detuning of the Rydberg state and studied the quantum phase transitions from disordered to ordered crystalline states of an 1D atomic array and realized $\mathbb{Z}_2$- and $\mathbb{Z}_3$-ordered states with the existence of a domain wall in $\mathbb{Z}_2$. Also, an incommensurate floating phase between $\mathbb{Z}_3$ and $\mathbb{Z}_4$ was obtained. We also investigated the effect of the sweeping rate on the probability of obtaining the $\mathbb{Z}_2$-ordered state and calculated the corresponding critical detuning and studied the domain walls. Further optimization of the generation of quantum phases of matter can include special design of composite laser pulses.

We considered solutions for the MIS and MWIS problems using arrays of ultracold neutral atoms excited to Rydberg states. We have obtained MISs and MWISs of planar and nonplanar graphs. For the MIS problem, we concluded that it is a geometry-constrained problem, and generation of the independent sets for the same geometric patterns have equal probabilities. For the MWIS problem the weights of each vertex change significantly the character of the resulting most probable independent set. The probabilities of MISs of the weighted graph are sort in descending order by the sum of weights of each set. The use of quantum wire can help mediate strong interactions of distant vertices. Also, quantum wires can be used to perform quantum annealing of non-unit-disk graphs. Using the heteronuclear structure of the atomic array, it is feasible to distinguish the measurement of atomic states representing the graph and the wire vertices due to the separation of the wavelengths and reduction of crosstalk among different chemical elements. Moreover, the cost Δ_f of finding the MIS or MWIS increases proportionally for longer lengths of quantum wires.

An incommensurate floating phase between $\bar{\mathbb{Z}}_2$ and $\bar{\mathbb{Z}}_3$ in the 2D atomic array, formed as a seven-pan graph representation, was realized, allowing us to use a quantum wire, which is not in the antiferromagnetic state, for a solution of the MWIS. This incommensurate phase does not exist in 1D arrays for equal detunings of transitions to the Rydberg state. The results of incommensurate phases can open new directions for realizing exotic states of matter.

Note added. Recently, we became aware of the foremost experimental demonstration of the weighted graphs, verifying the ability to prepare weighted graphs in 1D and 2D arrays [68].

Data sets supporting plots in this paper are available upon request from A.M.F.

ACKNOWLEDGMENTS

This work was supported by the Russian Science Foundation (Grant No. 23-42-00031). A.M.F. acknowledges financial support from the joint executive educational program between Egypt and Russia (Grant No. EGY-6544/19). P.X. acknowledges financial support from the National Key Research and Development Program of China (Grant No. 2021YFA1402001) and the National Natural Science Foundation of China (Grants No. 12261131507 and No. U20A2074).

[1] S. Arora and B. Barak, *Computational Complexity: A Modern Approach* (Cambridge University Press, Cambridge, 2009).

[2] N. Wagner, C. Poole, T. M. Graham, and M. Saffman, Benchmarking a neutral-atom quantum computer, Int. J. Quantum Inf. **22**, 2450001 (2024).

[3] M. Kim, K. Kim, J. Hwang, E.-G. Moon, and J. Ahn, Rydberg quantum wires for maximum independent set problems, Nat. Phys. **18**, 755 (2022).

[4] A. W. Glaetzle, R. M. van Bijnen, P. Zoller, and W. Lechner, A coherent quantum annealer with Rydberg atoms, Nat. Commun. **8**, 15813 (2017).

[5] J. A. Bondy and U. S. R. Murty, *Graph Theory with Applications* (North-Holland, Amsterdam, 1982).

[6] T. Graham, Y. Song, J. Scott, C. Poole, L. Phuttitarn, K. Jooya, P. Eichler, X. Jiang, A. Marra, B. Grinkemeyer *et al.*, Multi-qubit entanglement and algorithms on a neutral-atom quantum computer, Nature (London) **604**, 457 (2022).

[7] L. Zhou, S.-T. Wang, S. Choi, H. Pichler, and M. D. Lukin, Quantum approximate optimization algorithm: Performance, mechanism, and implementation on near-term devices, Phys. Rev. X **10**, 021067 (2020).

[8] M. H. Muñoz-Arias, S. Kourtis, and A. Blais, Low-depth Clifford circuits approximately solve MaxCut, Phys. Rev. Res. **6**, 023294 (2024).

[9] G. V. Paradezhenko, A. A. Pervishko, and D. Yudin, Probabilistic tensor optimization of quantum circuits for the max-k-cut problem, Phys. Rev. A **109**, 012436 (2024).

[10] L. T. Brady and S. Hadfield, Iterative quantum algorithms for maximum independent set: A tale of low-depth quantum algorithms, arXiv:2309.13110.

[11] J. R. Finžgar, A. Kerschbaumer, M. J. A. Schuetz, C. B. Mendl, and H. G. Katzgraber, Quantum-informed recursive optimization algorithms, PRX Quantum **5**, 020327 (2024).

[12] N. Bauer, K. Yeter-Aydeniz, E. Kokkas, and G. Siopsis, Solving power grid optimization problems with Rydberg atoms, arXiv:2404.11440.

[13] E. Farhi, J. Goldstone, S. Gutmann, and M. Sipser, Quantum computation by adiabatic evolution, arXiv:quant-ph/0001106.

[14] B. F. Schiffer, J. Tura, and J. I. Cirac, Adiabatic spectroscopy and a variational quantum adiabatic algorithm, PRX Quantum **3**, 020347 (2022).

[15] P. Scholl, M. Schuler, H. J. Williams, A. A. Eberharter, D. Barredo, K.-N. Schymik, V. Lienhard, L.-P. Henry, T. C. Lang, T. Lahaye *et al.*, Quantum simulation of 2D antiferromagnets with hundreds of Rydberg atoms, Nature (London) **595**, 233 (2021).

[16] S. Ebadi, T. T. Wang, H. Levine, A. Keesling, G. Semeghini, A. Omran, D. Bluvstein, R. Samajdar, H. Pichler, W. W. Ho *et al.*, Quantum phases of matter on a 256-atom programmable quantum simulator, Nature (London) **595**, 227 (2021).

[17] J. Taylor, S. Goswami, V. Walther, M. Spanner, C. Simon, and K. Heshami, Simulation of many-body dynamics using Rydberg excitons, Quantum Sci. Technol. **7**, 035016 (2022).

[18] S. Ebadi, A. Keesling, M. Cain, T. T. Wang, H. Levine, D. Bluvstein, G. Semeghini, A. Omran, J.-G. Liu, R. Samajdar *et al.*, Quantum optimization of maximum independent set using Rydberg atom arrays, Science **376**, 1209 (2022).

[19] D. Lykov, J. Wurtz, C. Poole, M. Saffman, T. Noel, and Y. Alexeev, Sampling frequency thresholds for the quantum advantage of the quantum approximate optimization algorithm, npj Quantum Inf. **9**, 73 (2023).

[20] R. S. Andrist, M. J. A. Schuetz, P. Minssen, R. Yalovetzky, S. Chakrabarti, D. Herman, N. Kumar, G. Salton, R. Shaydulin, Y. Sun, M. Pistoia, and H. G. Katzgraber, Hardness of the maximum-independent-set problem on unit-disk graphs and prospects for quantum speedups, Phys. Rev. Res. **5**, 043277 (2023).

[21] W. d. S. Coelho, M. D'Arcangelo, and L.-P. Henry, Efficient protocol for solving combinatorial graph problems on neutral-atom quantum processors, arXiv:2207.13030.

[22] J. Z. Lu, L. Jiao, K. Wolinski, M. Kornjača, H.-Y. Hu, S. Cantu, F. Liu, S. F. Yelin, and S.-T. Wang, Digital-analog quantum learning on Rydberg atom arrays, arXiv:2401.02940.

[23] A. Köse and M. Médard, *Proceedings of the 2017 IEEE 28th Annual International Symposium on Personal, Indoor, and Mobile Radio Communications, Montreal* (IEEE, Piscataway, 2017), pp. 1–7.

[24] J. R. Finžgar, M. J. A. Schuetz, J. K. Brubaker, H. Nishimori, and H. G. Katzgraber, Designing quantum annealing schedules using Bayesian optimization, Phys. Rev. Res. **6**, 023063 (2024).

[25] N. Przulj, in *Knowledge Discovery in Proteomics*, edited by I. Jurisica and D. Wigle (Chapman & Hall/CRC, Boca Raton, 2005), pp. 73–128.

[26] A. Byun, M. Kim, and J. Ahn, Finding the maximum independent sets of platonic graphs using Rydberg atoms, PRX Quantum **3**, 030305 (2022).

[27] C. Dalyac, L.-P. Henry, M. Kim, J. Ahn, and L. Henriet, Exploring the impact of graph locality for the resolution of the maximum-independent-set problem with neutral atom devices, Phys. Rev. A **108**, 052423 (2023).

[28] K. Kim, M. Kim, J. Park, A. Byun, and J. Ahn, Quantum computing dataset of maximum independent set problem on king lattice of over hundred Rydberg atoms, Sci. Data **11**, 111 (2024).

[29] B. F. Schiffer, D. S. Wild, N. Maskara, M. Cain, M. D. Lukin, and R. Samajdar, Circumventing superexponential runtimes for hard instances of quantum adiabatic optimization, Phys. Rev. Res. **6**, 013271 (2024).

[30] K. Goswami, R. Mukherjee, H. Ott, and P. Schmelcher, Solving optimization problems with local light-shift encoding on Rydberg quantum annealers, Phys. Rev. Res. **6**, 023031 (2024).

[31] H. Yeo, H. E. Kim, and K. Jeong, Approximating maximum independent set on Rydberg atom arrays using local detunings, arXiv:2402.09180.

[32] M.-T. Nguyen, J.-G. Liu, J. Wurtz, M. D. Lukin, S.-T. Wang, and H. Pichler, Quantum optimization with arbitrary connectivity using Rydberg atom arrays, PRX Quantum **4**, 010316 (2023).

[33] M. Lanthaler, C. Dlaska, K. Ender, and W. Lechner, Rydberg-blockade-based parity quantum optimization, Phys. Rev. Lett. **130**, 220601 (2023).

[34] I. I. Beterov and M. Saffman, Rydberg blockade, Förster resonances, and quantum state measurements with different atomic species, Phys. Rev. A **92**, 042710 (2015).

[35] I. Hen and M. S. Sarandy, Driver Hamiltonians for constrained optimization in quantum annealing, Phys. Rev. A **93**, 062312 (2016).

[36] I. D. Kivlichan, N. Wiebe, R. Babbush, and A. Aspuru-Guzik, Bounding the costs of quantum simulation of many-body physics in real space, J. Phys. A: Math. Theor. **50**, 305301 (2017).

[37] I. I. Beterov, M. Saffman, E. A. Yakshina, D. B. Tretyakov, V. M. Entin, S. Bergamini, E. A. Kuznetsova, and I. I. Ryabtsev, Two-qubit gates using adiabatic passage of the Stark-tuned Förster resonances in Rydberg atoms, Phys. Rev. A **94**, 062307 (2016).

[38] C. Mc Keever and M. Lubasch, Towards adiabatic quantum computing using compressed quantum circuits, PRX Quantum **5**, 020362 (2024).

[39] A. Browaeys and T. Lahaye, Many-body physics with individually controlled Rydberg atoms, Nat. Phys. **16**, 132 (2020).

[40] N. Šibalić, J. D. Pritchard, C. S. Adams, and K. J. Weatherill, ARC: An open-source library for calculating properties of alkali Rydberg atoms, Comput. Phys. Commun. **220**, 319 (2017).

[41] R. J. Leroy and R. B. Bernstein, Dissociation energies of diatomic moleculles from vibrational spacings of higher levels: Application to the halogens, Chem. Phys. Lett. **5**, 42 (1970).

[42] A. M. Farouk, I. I. Beterov, P. Xu, S. Bergamini, and I. I. Ryabtsev, Parallel implementation of $CNOT^N$ and C_2NOT^2 gates via homonuclear and heteronuclear Förster interactions of Rydberg atoms, Photonics **10**, 1280 (2023).

[43] H. Bernien, S. Schwartz, A. Keesling, H. Levine, A. Omran, H. Pichler, S. Choi, A. S. Zibrov, M. Endres, M. Greiner *et al.*, Probing many-body dynamics on a 51-atom quantum simulator, Nature (London) **551**, 579 (2017).

[44] A. Keesling, A. Omran, H. Levine, H. Bernien, H. Pichler, S. Choi, R. Samajdar, S. Schwartz, P. Silvi, S. Sachdev *et al.*, Quantum Kibble–Zurek mechanism and critical dynamics on a programmable Rydberg simulator, Nature (London) **568**, 207 (2019).

[45] F. Fang, K. Wang, V. S. Liu, Y. Wang, R. Cimmino, J. Wei, M. Bintz, A. Parr, J. Kemp, K.-K. Ni *et al.*, Probing critical phenomena in open quantum systems using atom arrays, arXiv:2402.15376.

[46] T. W. Kibble, Topology of cosmic domains and strings, J. Phys. A: Math. Gen. **9**, 1387 (1976).

[47] W. H. Zurek, Cosmological experiments in superfluid helium? Nature (London) **317**, 505 (1985).

[48] M. Anquez, B. A. Robbins, H. M. Bharath, M. Boguslawski, T. M. Hoang, and M. S. Chapman, Quantum Kibble-Zurek mechanism in a spin-1 Bose-Einstein condensate, Phys. Rev. Lett. **116**, 155301 (2016).

[49] G. Semeghini, H. Levine, A. Keesling, S. Ebadi, T. T. Wang, D. Bluvstein, R. Verresen, H. Pichler, M. Kalinowski, R. Samajdar *et al.*, Probing topological spin liquids on a programmable quantum simulator, Science **374**, 1242 (2021).

[50] W. H. Zurek, U. Dorner, and P. Zoller, Dynamics of a quantum phase transition, Phys. Rev. Lett. **95**, 105701 (2005).

[51] D. A. Huse and M. E. Fisher, Commensurate melting, domain walls, and dislocations, Phys. Rev. B **29**, 239 (1984).

[52] M. Rader and A. M. Läuchli, Floating phases in one-dimensional Rydberg Ising chains, arXiv:1908.02068.

[53] I. A. Maceira, N. Chepiga, and F. Mila, Conformal and chiral phase transitions in Rydberg chains, Phys. Rev. Res. **4**, 043102 (2022).

[54] J. Zhang, S. H. Cantú, F. Liu, A. Bylinskii, B. Braverman, F. Huber, J. Amato-Grill, A. Lukin, N. Gemelke, A. Keesling *et al.*, Probing quantum floating phases in Rydberg atom arrays, arXiv:2401.08087.

[55] J. Balewski, M. Kornjaca, K. Klymko, S. Darbha, M. R. Hirsbrunner, P. Lopes, F. Liu, and D. Camps, Engineering quantum states with neutral atoms, arXiv:2404.04411.

[56] P. Fendley, K. Sengupta, and S. Sachdev, Competing density-wave orders in a one-dimensional hard-boson model, Phys. Rev. B **69**, 075106 (2004).

[57] R. Samajdar, S. Choi, H. Pichler, M. D. Lukin, and S. Sachdev, Numerical study of the chiral $\mathbb{Z}_3$ quantum phase transition in one spatial dimension, Phys. Rev. A **98**, 023614 (2018).

[58] A. Byun, J. Jung, K. Kim, M. Kim, S. Jeong, H. Jeong, and J. Ahn, Rydberg-atom graphs for quadratic unconstrained binary optimization problems, Adv. Quantum Technol. **7**, 2300398 (2024).

[59] N. W. Johnson, Convex polyhedra with regular faces, Can. J. Math. **18**, 169 (1966).

[60] https://www.graphclasses.org/

[61] X. Qiu, P. Zoller, and X. Li, Programmable quantum annealing architectures with Ising quantum wires, PRX Quantum **1**, 020311 (2020).

[62] K. Singh, S. Anand, A. Pocklington, J. T. Kemp, and H. Bernien, Dual-element, two-dimensional atom array with continuous-mode operation, Phys. Rev. X **12**, 011040 (2022).

[63] S. Anand, C. E. Bradley, R. White, V. Ramesh, K. Singh, and H. Bernien, A dual-species Rydberg array, arXiv:2401.10325.

[64] A. M. Farouk, I. I. Beterov, P. Xu, and I. I. Ryabtsev, Scalable heteronuclear architecture of neutral atoms based on EIT, J. Exp. Theor. Phys. **137**, 202 (2023).

[65] P. M. Ireland, D. M. Walker, and J. D. Pritchard, Interspecies Förster resonances for Rb-Cs Rydberg d-states for enhanced multi-qubit gate fidelities, Phys. Rev. Res. **6**, 013293 (2024).

[66] F. Cesa and H. Pichler, Universal quantum computation in globally driven Rydberg atom arrays, Phys. Rev. Lett. **131**, 170601 (2023).

[67] The Rydberg blockade radius R_b of wire atoms is slightly different from the Rydberg blockade radius of graph atoms.

[68] A. de Oliveira, E. Diamond-Hitchcock, D. Walker, M. Wells-Pestell, G. Pelegrí, C. Picken, G. Malcolm, A. Daley, J. Bass, and J. Pritchard, Demonstration of weighted graph optimization on a Rydberg atom array using local light-shifts, arXiv:2404.02658.